PERGAMON

International Journal of Solids and Structures 38 (2001) 53–74

INTERNATIONAL JOURNAL OF SOLIDS and STRUCTURES

www.elsevier.com/locate/ijsolstr

Mechanical properties of isolation bearings identified by a viscoelastic model

Hsiang-Chuan Tsai *, Shaw-Jiun Hsueh

Department of Construction Engineering, National Taiwan University of Science and Technology, 43, Section 4, Keelung Road, Taipei, Taiwan, ROC

Received 10 March 1999; in revised form 25 November 1999

Abstract

The Haringx theory is usually employed to describe the mechanical behavior of rubber bearings subjected to a compressive axial load and a lateral shear deformation, but it does not consider the damping effect. In order to study the behavior of isolation bearings which possess an energy-dissipation capacity, the explicit formulas for the horizontal stiffness of viscoelastic columns and the corresponded height reduction are derived by the method of variable separation. These explicit formulas are then applied to develop an identification procedure to find the shear modulus and loss factor of the rubber using the cyclic shear tests of isolation bearings. Through this identification procedure, the empirical formulas for the shear modulus and the loss factor of rubber are established as functions of the strain amplitude and the excitation frequency.

Keywords: Base isolation; Elastomeric bearing; Viscoelastic column

1. Introduction

Base isolation is a technique for earthquake protection in which isolation bearings are installed in building foundations to reduce the damaging motion that horizontal earthquakes transmit to buildings. An isolation bearing consists of thin sheets of rubber bonded to interleaving steel plates, thus, providing sufficient vertical rigidity to sustain gravitational loading and yet allowing horizontal flexibility to shift the fundamental frequency of the isolated building away from the dominant frequency range of most earthquakes.

The deformation of isolation bearings is usually analyzed by Haringx's theory (Haringx, 1949; Kelly, 1993) which is an elastic beam theory considering the effects of axial loading and shear deformation. By this theory, the horizontal stiffness of the bearings is shown to decrease with an increase in the compressive axial load. However, most isolation bearings possess the capacity of energy dissipation, which cannot be simulated by the elastic column model utilized in Haringx's theory. Koh and Kelly (1986, 1989) previously used a viscoelastic column model to analyze the steady-state response of isolation bearings subjected to a sinusoidal horizontal force and a constant vertical load. They showed that increasing the compressive vertical

* Corresponding author. Fax: +886-2-2737-6606.

0020-7683/00/$ - see front matter
PII: S0020-7683(00)00010-X

load can enhance the energy dissipation of the viscoelastic column. Their solution was based on the mode superposition method and is an infinite series of complex numbers. Although they show that the convergence of the series is very rapid and the first term of the series already gives a good approximation, the form of complex numbers is not convenient for application. In this article, the horizontal stiffness and the corresponding loss angle of the viscoelastic column are solved by the method of variable separation and the formulas for these solutions are expressed in terms of real numbers, which are then applied to investigate the behavior of the columns under the excitation of sinusoidal shear forces and constant axial loads.

To define the stiffness and damping characteristics of isolation bearings requires a knowledge of the material properties of rubber. Although there is a standard test procedure to measure the shear modulus of rubber (ASTM, 1987), the properties of the rubber used in the bearings are somewhat different from the properties measured in the standard test due to different curing conditions and differences in specimen size between the isolation bearings and the specimens of standard test. By means of the theoretical solution of viscoelastic columns, a procedure to identify the shear modulus and loss factor of the rubber from the cyclic shear tests of isolation bearings is proposed in this article. Through this identification procedure, the dependence of the material properties on the strain amplitude and input frequency can be explored.

2. Theoretical model

2.1. Steady-state response

The deformation of a viscoelastic column of height h is shown in Fig. 1(a). The lower end of the column is fixed against any displacement and rotation, whereas the upper end is allowed to move horizontally and vertically but is still constrained against rotation. The x-axis denotes the centroidal axis of the column with the origin located at the bottom of the column. When the upper end of the column is subjected to a constant compressive force P and a time-varied horizontal force, $F(t)$, it will induce the bending moment $M(x,t)$ and shear force $V(x,t)$ at the cross-section of the height x as shown in Fig. 1(b). The moment equilibrium leads to

$$M(x,t) = M_0(t) - Pu(x,t) - F(t)x, \tag{1}$$

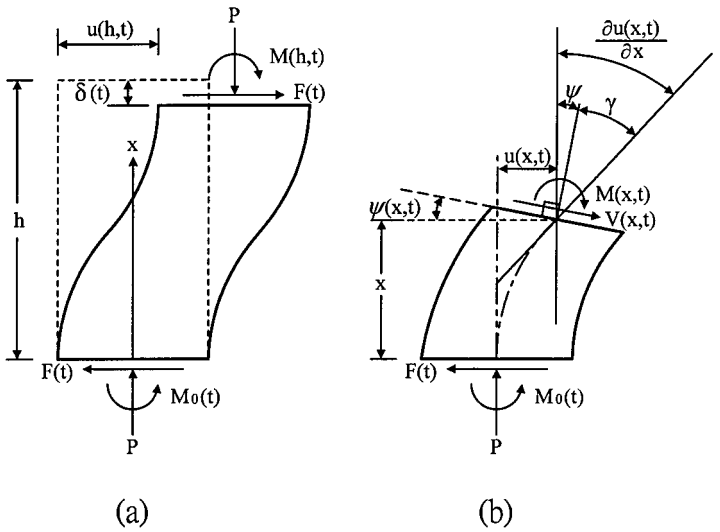

Fig. 1. Loading and deformation of the viscoelastic column at (a) upper end and (b) middle section.

where $u(x,t)$ is the horizontal displacement and $M_0(t)$ is the moment reaction at the lower end of the column. The equilibrium of horizontal forces gives

$$V(x,t) = F(t)\cos\psi(x,t) + P\sin\psi(x,t), \tag{2}$$

where $\psi(x,t)$ is the rotational angle of the cross-section. Considering the small magnitude of ψ, Eq. (2) can be approximated as

$$V(x,t) \doteq F(t) + P\psi(x,t). \tag{3}$$

The shear deformation $\gamma(x,t)$ is the difference between the rotation of the column axis $\partial u/\partial x$ and the rotation of the cross-section ψ:

$$\gamma(x,t) = \frac{\partial u(x,t)}{\partial x} - \psi(x,t). \tag{4}$$

When $F(t)$ is a sinusoidal excitation of amplitude F_0 and frequency ω and the response of the column reaches a steady state, then the exciting force can be expressed in a complex form as $F(t) = F_0 e^{i\omega t}$ and the induced deformations also have complex forms as

$$u(x,t) = u^*(x)e^{i\omega t}, \quad \psi(x,t) = \psi^*(x)e^{i\omega t}, \quad \gamma(x,t) = \gamma^*(x)e^{i\omega t}, \tag{5}$$

where the superscript * denotes the complex amplitude. The other force components in the steady state become

$$M(x,t) = M^*(x)e^{i\omega t}, \quad V(x,t) = V^*(x)e^{i\omega t}, \quad M_0(t) = M_0^* e^{i\omega t}. \tag{6}$$

Substituting Eqs. (5) and (6) into Eqs. (1) and (3), the equilibrium equations in the steady state become

$$M^*(x) = M_0^* - Pu^*(x) - F_0 x, \tag{7}$$

$$V^*(x) = F_0 + P\psi^*(x). \tag{8}$$

Also, the shear deformation in Eq. (4) becomes

$$\gamma^*(x) = \frac{du^*}{dx} - \psi^*(x). \tag{9}$$

The stress–strain relation of the viscoelastic material is usually expressed in terms of a complex form. Corresponding to Young's modulus E and the shear modulus G, respectively, the complex Young's modulus E^* and the complex shear modulus G^* are defined as

$$E^* = E(1 + i\eta), \qquad G^* = G(1 + i\eta), \tag{10}$$

where η is the loss factor of the material. When the response of the viscoelastic column reaches a steady state, the constitutive equation for bending moment can be expressed as

$$M^*(x) = E^* I_s \frac{d\psi^*(x)}{dx}, \tag{11}$$

where I_s is the moment of the cross-sectional inertial. The constitutive equation for shear deformation becomes

$$V^*(x) = G^* A_s \gamma^*(x), \tag{12}$$

where A_s is the shear area.

Substituting Eqs. (8) and (9) into Eq. (12) gives the relation between the horizontal displacement and the cross-sectional rotation,

$$\frac{\mathrm{d}u^*}{\mathrm{d}x} = \left(1 + \frac{P}{G^* A_s}\right)\psi^* + \frac{F_0}{G^* A_s}. \tag{13}$$

Substituting Eq. (11) into Eq. (7), the moment equilibrium becomes

$$E^* I_s \frac{\mathrm{d}\psi^*}{\mathrm{d}x} = M_0^* - Pu^* - F_0 x. \tag{14}$$

Substituting Eq. (13) into the derivative of the above equation with respect to x, we obtain a complex differential equation

$$\left(\frac{E^* I_s}{1 + \frac{P}{G^* A_s}}\right)\frac{\mathrm{d}^2\psi^*}{\mathrm{d}x^2} + P\psi^* = -F_0. \tag{15}$$

Satisfying the steady-state boundary conditions, $\psi^*(0) = 0$ and $\psi^*(h) = 0$, the complex amplitude of cross-sectional rotation can be solved from Eq. (15):

$$\psi^*(x) = \frac{F_0}{P}\left[-1 + \cos\left(\frac{\alpha^* x}{h}\right) + \left(\frac{1 - \cos\alpha^*}{\sin\alpha^*}\right)\sin\left(\frac{\alpha^* x}{h}\right)\right], \tag{16}$$

where α^* is a complex parameter defined as

$$\alpha^* = h\left[\frac{P}{E^* I_s}\left(1 + \frac{P}{G^* A_s}\right)\right]^{1/2}. \tag{17}$$

Substituting Eq. (16) into Eq. (13) and integrating with respect to x, the complex amplitude of horizontal displacement can be solved by satisfying the steady-state boundary condition $u^*(0) = 0$

$$u^*(x) = \frac{F_0 h}{P\alpha^*}\left\{\left(1 + \frac{P}{G^* A_s}\right)\left[\left(\frac{1 - \cos\alpha^*}{\sin\alpha^*}\right)\left(1 - \cos\left(\frac{\alpha^* x}{h}\right)\right) + \sin\left(\frac{\alpha^* x}{h}\right)\right] - \frac{\alpha^* x}{h}\right\}. \tag{18}$$

2.2. Horizontal stiffness

The amplitude ratio of the horizontal applied force to the horizontal displacement at the top of the column represents the horizontal stiffness of the viscoelastic column, which can be derived from Eq. (18)

$$K_h^* = \frac{F_0}{u^*(h)} = \frac{P}{h}\left[\frac{\alpha^*}{(1 + \frac{P}{G^* A_s})(2\tan\frac{\alpha^*}{2}) - \alpha^*}\right]. \tag{19}$$

The above horizontal stiffness is a complex quantity, of which a split form is more convenient in engineering applications, that is

$$K_h^* = K_r + \mathrm{i}K_i, \tag{20}$$

where K_r, the real part of K_h^*, is referred to as the storage stiffness and K_i, the imaginary part of K_h^*, is called the loss stiffness.

Before finding the expressions of K_r and K_i, the real and imaginary parts of α^* defined in Eq. (17) have to be solved. Let ρ denote the ratio of the bending rigidity to shear rigidity,

$$\rho = \frac{EI_s}{GA_s h^2}. \tag{21}$$

Also, let the coefficients α and β be defined as

$$\alpha = \sqrt{\frac{1}{\rho}\left(1+\frac{P}{GA_s}\right)\frac{P}{GA_s}}, \qquad \beta = \frac{1}{1+\frac{P}{GA_s}}. \tag{22}$$

Applying the theory of complex variables, α^* in Eq. (17) can be split as

$$\alpha^* = \alpha(A - \mathrm{i}B), \tag{23}$$

where A and B are defined as

$$A = \frac{a+\eta b}{1+\eta^2}, \qquad B = \frac{\eta a - b}{1+\eta^2} \tag{24}$$

with

$$a = \sqrt{\frac{\sqrt{1+\beta^2\eta^2}+1}{2}}, \qquad b = \sqrt{\frac{\sqrt{1+\beta^2\eta^2}-1}{2}}. \tag{25}$$

Substituting Eq. (23) into Eq. (19), the real part of K_h^* is found as

$$K_r = \left(\frac{P\alpha\beta}{h}\right)\frac{\Gamma_r}{\Gamma_r^2+\Gamma_i^2} \tag{26}$$

and the imaginary part as

$$K_i = \left(\frac{P\alpha\beta}{h}\right)\frac{\Gamma_i}{\Gamma_r^2+\Gamma_i^2}, \tag{27}$$

where Γ_r is defined as

$$\Gamma_r = 2\frac{a\sin(\alpha A)+b\sinh(\alpha B)}{\cos(\alpha A)+\cosh(\alpha B)} - \alpha\beta \tag{28}$$

and Γ_i is defined as

$$\Gamma_i = 2\frac{a\sinh(\alpha B)-b\sin(\alpha A)}{\cos(\alpha A)+\cosh(\alpha B)}. \tag{29}$$

By means of Eq. (26), the variations of the storage stiffness with compressive force for different rigidity ratios and loss factors can be computed and are plotted in Fig. 2, which reveals that the storage stiffness decreases with increasing compressive force. When the storage stiffness equals zero, the viscoelastic column becomes unstable and the corresponding compressive force is referred to as buckling load. Fig. 2 also shows that increasing the rigidity ratio or loss factor will increase the storage stiffness. Using Eq. (27), the variations of the loss stiffness with compressive force for different rigidity ratios and loss factors until reaching the buckling load are plotted in Fig. 3, which shows that the loss stiffness increases with increasing compressive force. Increasing the rigidity ratio or decreasing the loss factor will reduce the loss stiffness.

The complex horizontal stiffness can also be expressed as

$$K_h^* = |K_h^*|\mathrm{e}^{\mathrm{i}\phi} \tag{30}$$

where $|K_h^*|$ is the stiffness magnitude and ϕ is the loss angle. According to Eqs. (26) and (27)

$$|K_h^*| = \left(\frac{P\alpha\beta}{h}\right)\frac{1}{\sqrt{\Gamma_r^2+\Gamma_i^2}}, \tag{31}$$

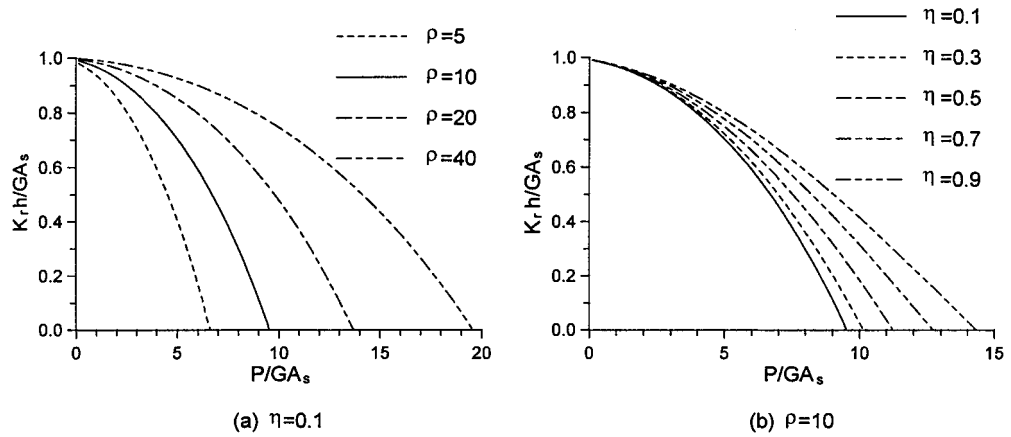

Fig. 2. Variation of storage stiffness with compressive force for different (a) rigidity ratios and (b) loss factors.

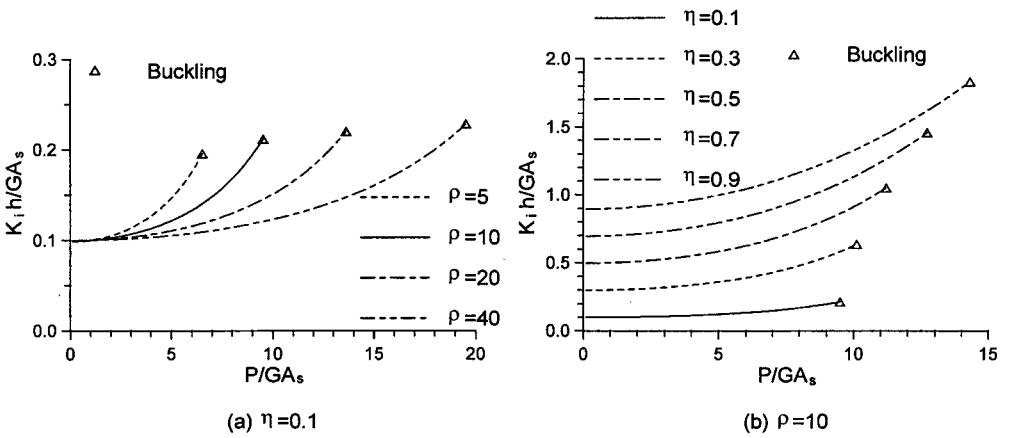

Fig. 3. Variation of loss stiffness with compressive force for different (a) rigidity ratios and (b) loss factors.

$$\phi = \tan^{-1}\frac{\Gamma_i}{\Gamma_r}. \tag{32}$$

The variations of stiffness magnitude with compressive force for different rigidity ratios and loss factors are plotted in Fig. 4, which reveals that the stiffness magnitude initially decreases and then increases with increasing compressive force. This decreasing tendency becomes less obvious when the loss factor is high. Higher rigidity ratio or loss factor indicates a higher stiffness magnitude. Fig. 5 shows the variations of loss angle with compressive force for different rigidity ratios and loss factors, indicating that the loss angle increases with increasing compressive force. In addition, a higher rigidity ratio has a smaller loss angle. When the compressive force is small, increasing the loss factor will increase the loss angle, although this tendency becomes reversed when the compressive force is close to the buckling load.

When $\eta = 0$, Eq. (28) becomes $\Gamma_r = 2\tan(\alpha/2) - \alpha\beta$, and Eq. (29) is $\Gamma_i = 0$. Substituting these Γ_r and Γ_i into Eqs. (26) and (27) leads to

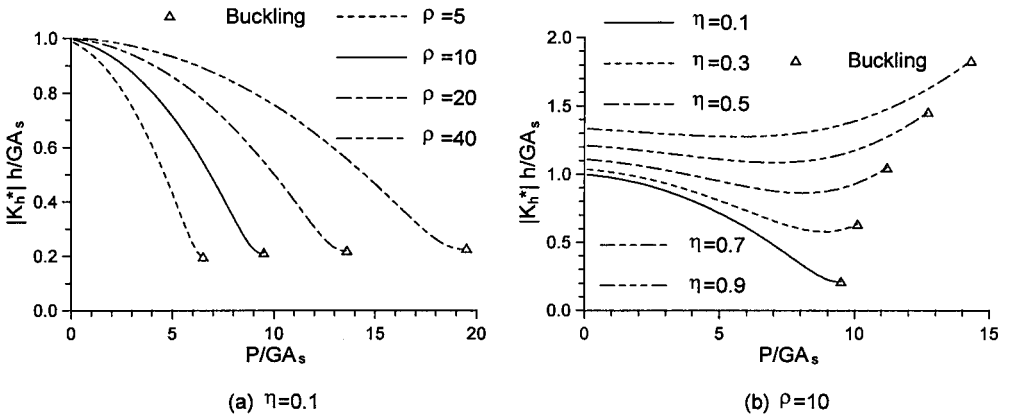

Fig. 4. Variation of stiffness magnitude with compressive force for different (a) rigidity ratios and (b) loss factors.

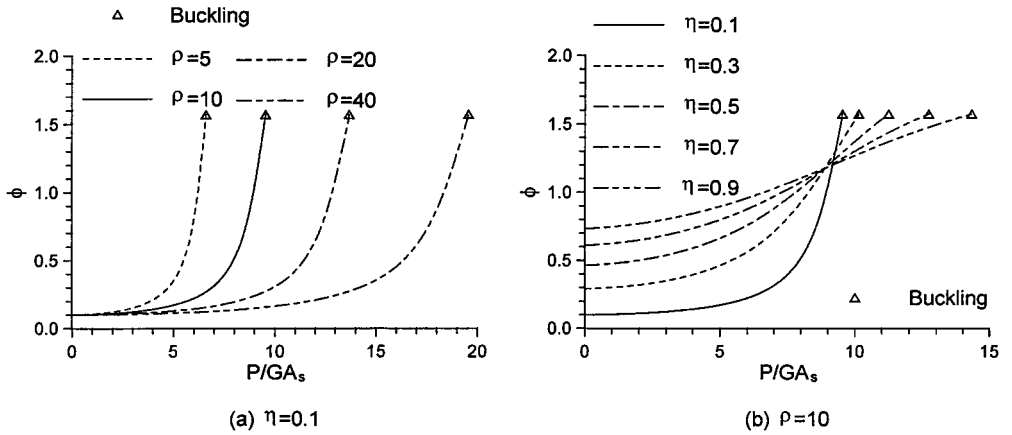

Fig. 5. Variation of loss angle with compressive force for different (a) rigidity ratios and (b) loss factors.

$$K_{\mathrm{h}}^{*} = K_{\mathrm{r}} = \frac{P}{h}\frac{\alpha\beta}{2\tan\frac{z}{2} - \alpha\beta}, \tag{33}$$

which is the horizontal stiffness of the elastic column without damping as derived by Haringx's theory (Kelly, 1993).

2.3. Hysteresis loops

If the horizontal force acting on the upper end of the viscoelastic column is $F(t) = F_0 \sin \omega t$, which is the imaginary part of $F_0 e^{i\omega t}$, the horizontal displacement at the upper end of the column becomes

$$u(h,t) = \frac{F_0}{|K_{\mathrm{h}}^{*}|}\sin(\omega t - \phi). \tag{34}$$

Thus, the stiffness magnitude is equal to the ratio of the maximum horizontal force to the maximum horizontal displacement

$$|K_{\mathrm{h}}^{*}| = \frac{F_0}{u_0}, \tag{35}$$

where u_0 denotes the amplitude of $u(h,t)$.

The time functions $F(t)$ and $u(h,t)$ have a phase difference ϕ. The curves related to these two quantities, shown in Fig. 6, form hysteresis loops. The tangential slope of hysteresis loops can be derived as

$$\frac{\mathrm{d}F}{\mathrm{d}u} = \frac{F_0}{u_0}\left[\cos\phi - \frac{\frac{u}{u_0}}{\sqrt{1-\left(\frac{u}{u_0}\right)^2}}\sin\phi\right], \tag{36}$$

which indicates

$$\left.\frac{\mathrm{d}F}{\mathrm{d}u}\right|_{u=0} = \frac{F_0}{u_0}\cos\phi = |K_{\mathrm{h}}^{*}|\cos\phi = K_{\mathrm{r}}. \tag{37}$$

Therefore, the storage stiffness is equal to the tangential slope of the hysteresis loop at $u(h,t)=0$. The hysteresis loops for the column of $\rho = 10$, $\eta = 0.1$ and $u_0/h = 1$ under different compressive forces are plotted in Fig. 6(a) which shows that increasing the compressive force reduces the inclination of loops. When the compressive force is equal to the buckling load, the storage stiffness is zero, so that the tangential slope of the hysteresis loop at $u = 0$ is zero, which is the case of $P/GA_{\mathrm{s}} = 9.525$ in Fig. 6(a).

The area of a hysteresis loop represents the energy dissipated in a loading cycle,

$$A_{\mathrm{loop}} = \oint F\,\mathrm{d}u = \pi F_0 u_0 \sin\phi = \pi u_0^2 K_{\mathrm{i}} \tag{38}$$

which indicates that the loss stiffness is an index of energy dissipation. The hysteresis loops plotted in Fig. 6(b) for the columns of different loss factors η reveal that higher values of η have larger loop areas, which is consistent with the phenomenon shown in Fig. 3(b) of higher values of η having higher values for K_{i}. It should be noted that the loss angle ϕ does not exactly represent energy dissipation. According to Eq. (38)

$$\phi = \sin^{-1}\frac{A_{\mathrm{loop}}}{\pi|K_{\mathrm{h}}^{*}|u_0^2}, \tag{39}$$

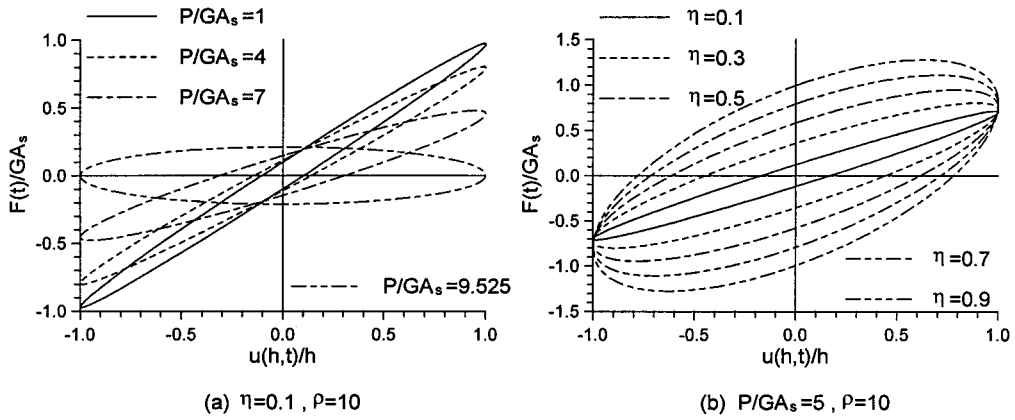

Fig. 6. Hysteresis loops of horizontal displacement ($u_0 = h$) for different (a) compressive forces and (b) loss factors.

which implies that the stiffness magnitude $|K_h^*|$ may affect the phase angle ϕ. In Fig. 5(b), when the compressive force is close to the buckling load, the column with a higher η has a smaller ϕ because the column with larger η has much higher $|K_h^*|$, as shown in Fig. 4(b).

2.4. Buckling load

When the compressive force is equal to the buckling load, the storage stiffness becomes zero. Thus, according to Eqs. (26) and (28), the buckling load P_{cr} is the smallest positive root of the variable P in the equation

$$\Gamma_r(P) = 2\frac{a\sin(\alpha A) + b\sinh(\alpha B)}{\cos(\alpha A) + \cosh(\alpha B)} - \alpha\beta = 0. \tag{40}$$

Because $\Gamma_r(P)$ is a nonlinear function of P, the analytical form of P_{cr} cannot be explicitly solved.

When $\eta = 0$, Eq. (40) becomes

$$2\tan\frac{\alpha}{2} - \alpha\beta = 0. \tag{41}$$

Based on Eq. (33), zero storage stiffness occurs at $\alpha = \pi$, but the buckling load solved from Eq. (41) leads to an infinite value for the storage stiffness, which seems to conflict with the definition of buckling load. Fig. 7 plots the curves of $\Gamma_r(P)$ in Eq. (40) for different loss factors with $\rho = 10$, showing that, as η is closer to zero, the slope of the curve near $\Gamma_r = 0$ becomes steeper and the peak value of Γ_r becomes higher. It can be deduced that, when $\eta = 0$, the P value corresponding to the point of $\Gamma_r = 0$ asymptotically becomes the same P value corresponding to the point of $\Gamma_r = \infty$, which can explain the conflicting phenomenon mentioned above. Assigning $\alpha = \pi$ to the formula of α in Eq. (22), the buckling load at $\eta = 0$ can be solved as

$$P_{cr} = \frac{GA_s}{2}\left(\sqrt{1 + 4\pi^2\rho} - 1\right), \tag{42}$$

which is the bucking load of the elastic column without damping.

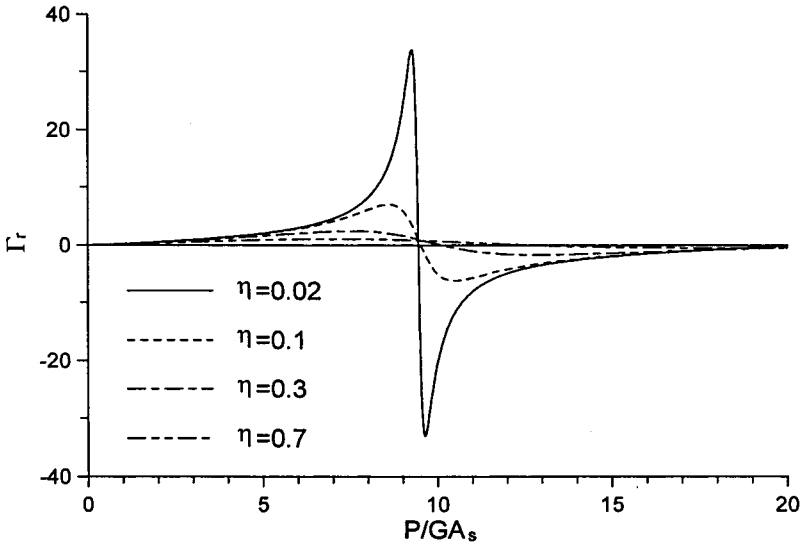

Fig. 7. Equation curves to solve buckling load ($\rho = 10$).

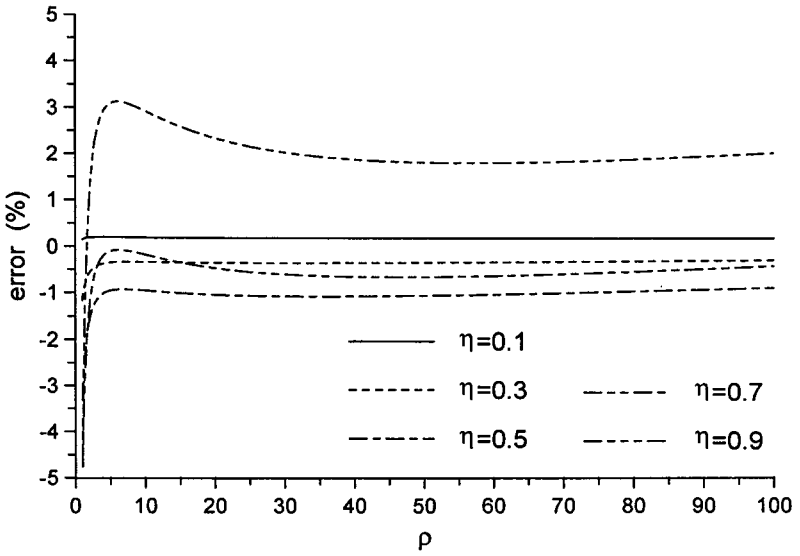

Fig. 8. Errors of empirical formula for buckling load.

Although the analytical solution of P_{cr} cannot be obtained from Eq. (40), numerical methods can be applied to calculate the values of P_{cr} for different η and ρ, and then, utilizing curve-fitting schemes, the empirical formula of P_{cr} can be established as

$$\frac{P_{cr}}{GA_s} \approx \tfrac{1}{2}\left(\sqrt{1+4\pi^2\rho}-1\right) + (0.01090 + 0.1142\sqrt{\rho})\eta + (-1.825 + 2.400\sqrt{\rho} + 0.006066\rho)\eta^2 + 0.03442\rho\eta^3. \tag{43}$$

The error in the above formula for the exact value of P_{cr} is plotted in Fig. 8, showing that, when ρ is between 1 and 100 and η is smaller than 0.9, the maximum error of the empirical formula is less than 5%. When $\eta = 0$, the empirical formula takes the form of Eq. (42).

2.5. Height reduction

Height reduction induced by the horizontal displacement of isolation bearing pads is an important parameter in the design of the base-isolation system (Kelly and Beucke, 1983). Fig. 9 shows the height reduction of a column element dx, where δ_1 is the vertical displacement induced by the cross-sectional rotation ψ

$$\delta_1 = \mathrm{d}x(1-\cos\psi), \tag{44}$$

and δ_2 is the vertical displacement caused by the shear deformation γ

$$\delta_2 = (\mathrm{d}x\tan\gamma)\sin\psi. \tag{45}$$

Applying Eq. (4) and considering the small magnitudes of ψ and γ, the height reduction of the column element can be approximated as

$$\mathrm{d}\delta = \delta_1 + \delta_2 \approx \psi\left(\frac{\mathrm{d}u}{\mathrm{d}x} - \tfrac{1}{2}\psi\right)\mathrm{d}x. \tag{46}$$

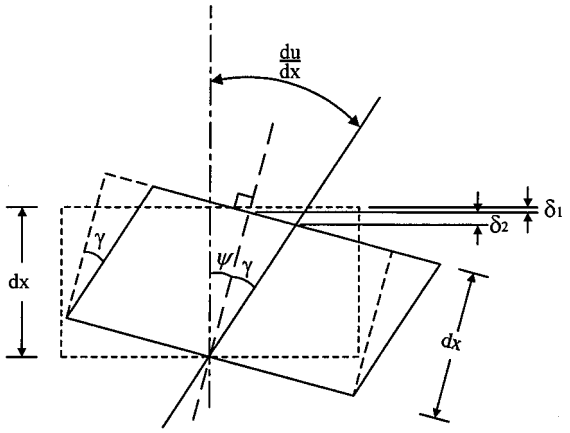

Fig. 9. Height reduction induced by bending and shear deformations.

The total height reduction at the upper end of the column is

$$\delta = \int_0^h \psi\left(\frac{\mathrm{d}u}{\mathrm{d}x} - \frac{1}{2}\psi\right)\mathrm{d}x, \tag{47}$$

which is the same equation derived by the energy approach (Koh and Kelly, 1986).

If the horizontal force is $F(t) = F_0 \sin \omega t$, the time function of the height reduction at the upper end of the viscoelastic column can be derived by a lengthy integration of Eq. (47)

$$\delta(t) = h\left(\frac{F_0}{P}\right)^2\left[g_1 - \sqrt{g_2^2 + g_3^2}\cos\left(2\omega t + \tan^{-1}\left(\frac{g_3}{g_2}\right)\right)\right] \tag{48}$$

in which g_1, g_2 and g_3 are defined as

$$g_1 = f_\mathrm{r}(d_5 - 4d_3) - f_\mathrm{i}(4d_4) - 2d_3 + \tfrac{1}{4}, \tag{49}$$

$$g_2 = f_\mathrm{r}\left(c_1d_1 + c_2d_2 - c_3d_3 - c_4d_4 + \tfrac{1}{2}\right) + f_\mathrm{i}(c_2d_1 - c_1d_2 + c_4d_3 - c_3d_4) - 2d_3 + \tfrac{1}{4}, \tag{50}$$

$$g_3 = -f_\mathrm{r}(c_2d_1 - c_1d_2 + c_4d_3 - c_3d_4) + f_\mathrm{i}\left(c_1d_1 + c_2d_2 - c_3d_3 - c_4d_4 + \tfrac{1}{2}\right) + 2d_4 \tag{51}$$

with f_r and f_i being

$$f_\mathrm{r} = \frac{P}{GA_\mathrm{s}}\frac{1}{1+\eta^2} + \frac{1}{2}, \tag{52}$$

$$f_\mathrm{i} = -\frac{P}{GA_\mathrm{s}}\frac{\eta}{1+\eta^2}, \tag{53}$$

c_1, c_2, c_3 and c_4 being

$$c_1 = \frac{1 + \cos(\alpha A)\cosh(\alpha B)}{(\cos(\alpha A) + \cosh(\alpha B))^2} - 1, \tag{54}$$

$$c_2 = \frac{\sin(\alpha A)\sinh(\alpha B)}{(\cos(\alpha A) + \cosh(\alpha B))^2}, \tag{55}$$

$$c_3 = 3 + \cos(2\alpha A)\cosh(2\alpha B), \tag{56}$$

$$c_4 = \sin(2\alpha A)\sinh(2\alpha B), \tag{57}$$

and d_1, d_2, d_3, d_4 and d_5 being

$$d_1 = \frac{1}{2} - \frac{A\sin(2\alpha A)\cosh(2\alpha B) + B\cos(2\alpha A)\sinh(2\alpha B)}{4\alpha(A^2+B^2)}, \tag{58}$$

$$d_2 = \frac{A\cos(2\alpha A)\sinh(2\alpha B) - B\sin(2\alpha A)\cosh(2\alpha B)}{4\alpha(A^2+B^2)}, \tag{59}$$

$$d_3 = \frac{A\sin(\alpha A) + B\sinh(\alpha B)}{4\alpha(A^2+B^2)(\cos(\alpha A)+\cosh(\alpha B))}, \tag{60}$$

$$d_4 = \frac{A\sinh(\alpha B) - B\sin(\alpha A)}{4\alpha(A^2+B^2)(\cos(\alpha A)+\cosh(\alpha B))}, \tag{61}$$

$$d_5 = \frac{1}{2\alpha(\cos(\alpha A)+\cosh(\alpha B))}\left(\frac{\sin(\alpha A)}{A} + \frac{\sinh(\alpha B)}{B}\right). \tag{62}$$

Thus, the maximum magnitude of the height reduction in Eq. (48) is

$$\delta_{\max} = h\left(\frac{F_0}{P}\right)^2\left(|g_1| + \sqrt{g_2^2+g_3^2}\right). \tag{63}$$

The maximum height reductions calculated from the above equation shows that, subjected to the same compressive force and the same amplitude of horizontal displacement, columns of a smaller rigidity ratio ρ or a smaller loss factor η have a higher height reduction.

3. Property identification

3.1. Bearing specimens and testing apparatus

Two groups of isolation bearings were used in the cyclic shear tests. One group of bearings were made of high-damping rubber and the other group of bearings were made of normal rubber, which has a lower damping value. The dimensions for the two groups of bearings were identical. Each group had two shapes: circular and square. The circular bearings, whose dimensions are shown in Fig. 10, have 20 thin rubber layers with thickness $t = 10$ mm and 19 steel shims which are 2 mm thick. The total rubber thickness is $t_r = 200$ mm and the height of the bearing excluding the end plates is $h = 238$ mm. The shim diameter is $d = 280$ mm and there is 10 mm of cover for a total diameter of 300 mm. The square bearings, whose dimensions are shown in Fig. 11, have the same number of rubber layers and steel shims as do the circular bearings, but the thickness of the rubber layers is $t = 6$ mm. The total rubber thickness is $t_r = 120$ mm and the height of the bearing excluding the end plates is $h = 158$ mm. The square shim has a side length $s = 180$ mm. Including 10 mm of cover, the total side length is 200 mm. Both shapes of bearings have oversize end plates which permit them to be bolted to the test rig.

The shear area related to the shear stiffness of bearings is defined as

$$A_s = A_0 + A_i\frac{h}{t_r}, \tag{64}$$

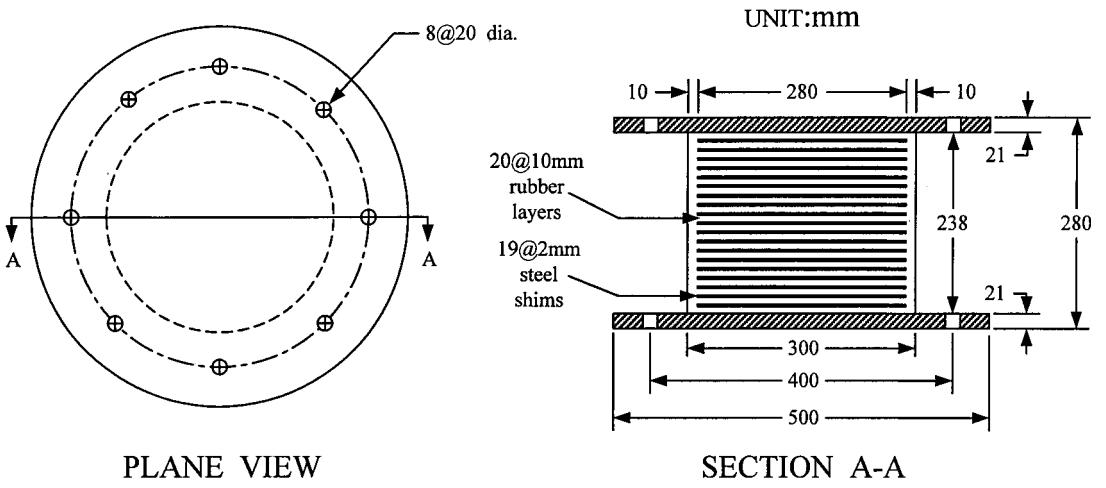

Fig. 10. Dimensions of circular bearings.

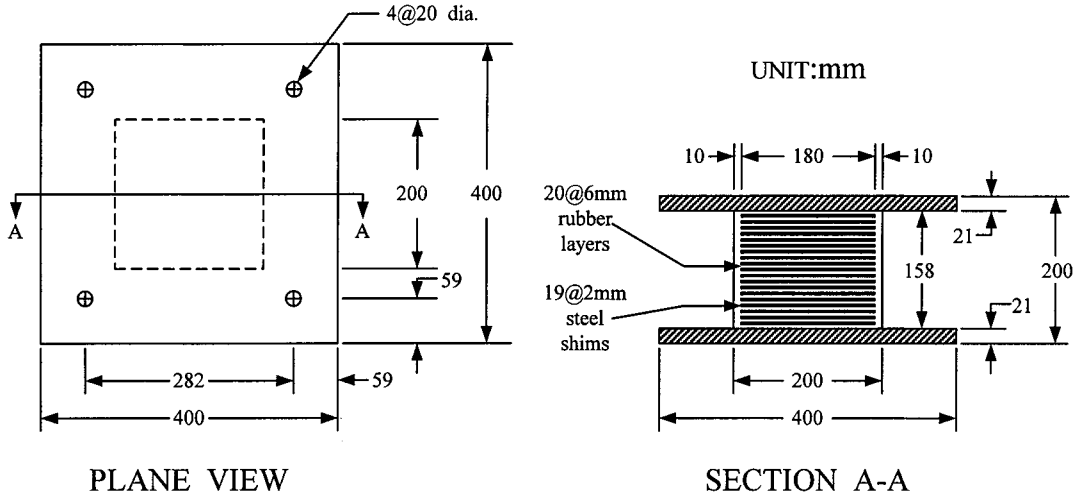

Fig. 11. Dimensions of square bearings.

where A_0 is the cross-sectional area of the cover rubber and A_i is the area of a rubber layer bonded to a steel shim. The shear stiffness of the cover rubber is included because of its bonding with the end plates. Multiplying A_i by h/t_r is needed to account for the fact that the steel shim does not deform in the composite system (Kelly, 1993).

The bending stiffness of a single layer of rubber bonded between two rigid plates has been derived as (Gent and Meinecke, 1970)

$$(EI)_{\text{eff}} = 3G\left(\frac{\pi d^4}{64}\right)\left(1+\frac{2}{3}\left(\frac{d}{4t}\right)^2\right) \tag{65}$$

for a circular rubber layer of diameter d and

$$(EI)_{\text{eff}} = 3G\left(\frac{s^4}{12}\right)\left(1 + 0.7424\left(\frac{s}{4t}\right)^2\right) \tag{66}$$

for a square rubber layer of side length s. For multiple-layered rubber bearings, the above stiffness must be modified in the same way as the shear stiffness to account for the presence of the steel shims (Kelly, 1993),

$$EI_{\text{s}} = (EI)_{\text{eff}}\frac{h}{t_{\text{r}}}. \tag{67}$$

Assigning the dimensions of the circular bearing and the square bearing into Eqs. (64)–(67), the ratios of bending stiffness to shear stiffness defined in Eq. (21) are calculated to be $\rho = 7.77$ for the circular bearings and $\rho = 11.78$ for the square bearings, which are independent of the material properties.

The testing apparatus for the cyclic shear test of isolation bearings is shown in Fig. 12. As the ends of a bearing specimen have to sustain the vertical compressive force and simultaneously allow the horizontal movement at one end during the test, the test rig requires a pair of identical bearing specimens for each test. The lower end of the lower bearing is fixed to the ground and the upper end of the upper bearing is connected to a vertical hydraulic actuator. During the test, the vertical actuator applies a constant compressive force to the bearings. A horizontal hydraulic actuator is connected with the specimens at the junction of the two bearings. The motion of the horizontal actuator follows the command signal from a controller. By giving the displacement amplitude and frequency to the controller, the horizontal actuator can move sinusoidally. The horizontal force and movement are measured, respectively, by the load cell and the linear variable differential transformer (LVDT) built into the horizontal actuator. The vertical force is measured by the load cell attached to the vertical actuator. An external LVDT is mounted at the top of the upper bearing to measure the vertical displacement. As the upper bearing and the lower bearing have the same lateral deformation shape, the horizontal force applied to one bearing specimen is equal to one half of the measured horizontal force; and the vertical deformation of one bearing specimen is equal to one half of the measured vertical displacement. In the experimental program, two pairs of the isolation bearings, called sample A and sample B, were tested for each rubber material and each shape of the bearings. Therefore, the material properties for each type of rubbers are identified from the tests of eight bearings.

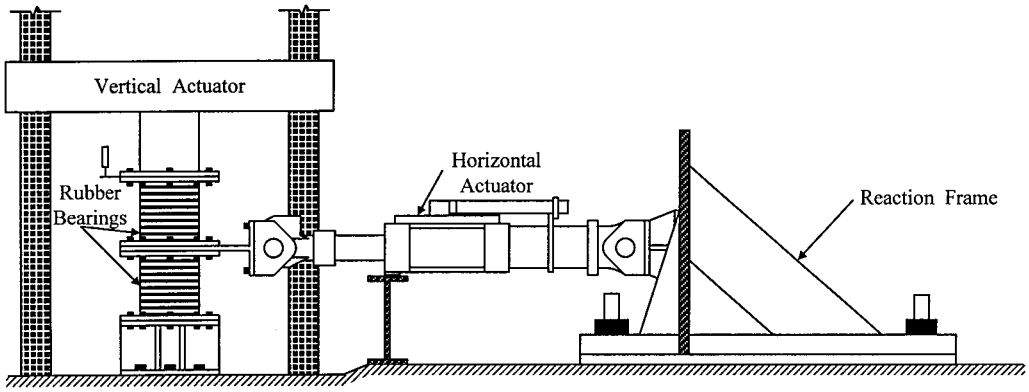

Fig. 12. Test rig for cyclic shear test of isolation bearings.

3.2. High-damping rubber bearings

It is known (Cole, 1979; Kelly and Celebi, 1984) that the mechanical properties of rubber depend on the amplitude of motion. In other words, the shear modulus G and the loss factor η of rubber may vary with the displacement amplitude u_0 in cyclic shear tests. However, during cyclic motion of a particular amplitude, the mechanical properties can be assumed as constants, so that we can apply the theoretical model of viscoelastic column to identify the dependence of the shear modulus G and the loss factor η on the maximum shear strain $\gamma_{\max}$, which is related to the displacement amplitude through $\gamma_{\max} = u_0/t_r$.

The isolation bearings were tested under different vertical loads and different horizontal displacement amplitudes. Through the measured horizontal force and displacement histories, the stiffness magnitude and loss angle of the bearings under a specified compressive force and a specified maximum shear strain can be calculated from Eqs. (35) and (39). Fig. 13 shows the stiffness magnitudes and the loss angles for the circular bearings of high-damping rubber under different compressive forces at $\gamma_{\max} = 0.75$. Also plotted in Fig. 13 are the theoretical curves of $|K_h^*|$ calculated from Eq. (31) and ϕ calculated from Eq. (32) using the dimensions of circular bearing and the identified properties $G = 0.611$ MPa and $\eta = 0.115$. This figure reveals that the variations of the stiffness magnitude and loss angle of isolation bearings with compressive force obtained from the experiments are very close to the curves predicted by the theoretical model of the viscoelastic column.

To obtain the identified properties G and η, an iterative procedure must be applied. At first, set $\eta = 0$ and assume different G values to calculate the theoretical curves of $|K_h^*|$ to fit the experimental values shown in Fig. 13(a). Apply the least square method to find the best fitting curve, and the corresponding G value is the shear modulus identified in the first iteration. Use this G value and assume different η values to calculate the theoretical curves of ϕ to fit the experimental values shown in Fig. 13(b). The η value of the best fitting curve obtained by the least square method is the loss factor identified in the first iteration. Based on the values for G and η identified in the first iteration, the second iteration can be carried out by the same process. The iteration procedure is continued until the identified parameters converge. Fig. 14 shows the convergence of the identified properties listed in Fig. 13. In general, only three or four iterations are required to reach the convergence.

The shear moduli and loss factors identified from the cyclic shear tests on the circular and square bearings of high-damping rubber for different maximum shear strains are shown in Fig. 15. It shows that the shear modulus of the high-damping rubber decreases with increasing the maximum shear strain. The

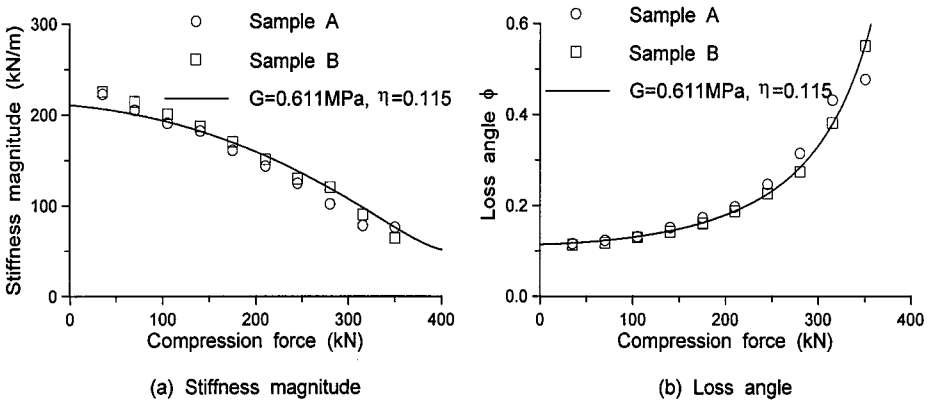

Fig. 13. (a) Stiffness magnitude and (b) loss angle of circular bearing of high-damping rubber varied with compressive force at $\gamma_{\max} = 0.75$.

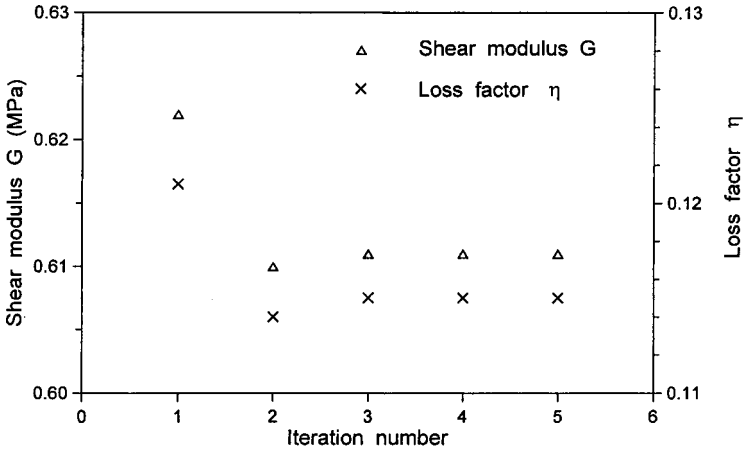

Fig. 14. Convergence of identified properties of high-damping rubber during iteration.

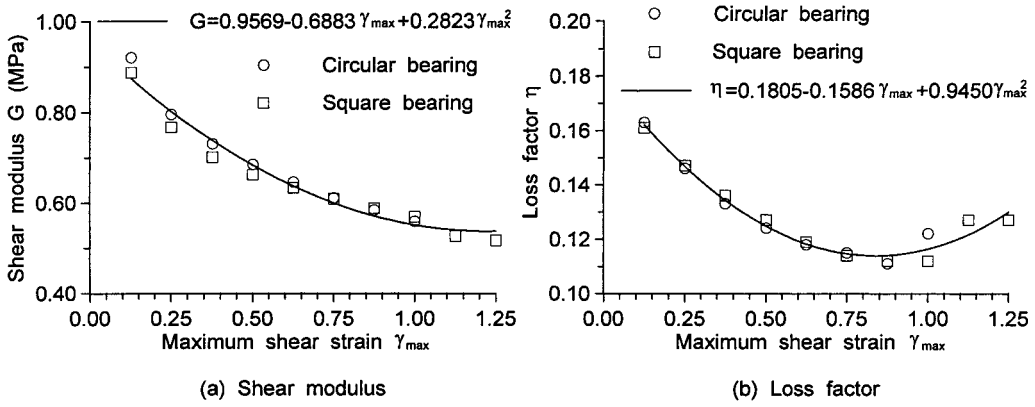

Fig. 15. (a) Shear modulus and (b) loss factor of high-damping rubber varied with maximum shear strain.

loss factor of the high-damping rubber has the same tendency for a smaller strain amplitude, but it starts to increase with increasing the maximum shear strain for a larger strain amplitude. The quadratic regression for the shear moduli shown in Fig. 15(a) is

$$G = 0.9569 - 0.6883\gamma_{\max} + 0.2823\gamma_{\max}^2. \tag{68}$$

The quadratic regression for the loss factors shown in Fig. 15(b) is

$$\eta = 0.1805 - 0.1586\gamma_{\max} + 0.09450\gamma_{\max}^2. \tag{69}$$

Substituting Eqs. (68) and (69) into Eqs. (31) and (32), the stiffness magnitude and loss angle become functions of the maximum shear strain, which are plotted in Fig. 16 for the circular bearing of high-damping rubber under the compressive force $P = 140$ kN. The data measured from the cyclic shear tests are also plotted in this figure and shown to be consistent with the theoretical model using the material properties of regression.

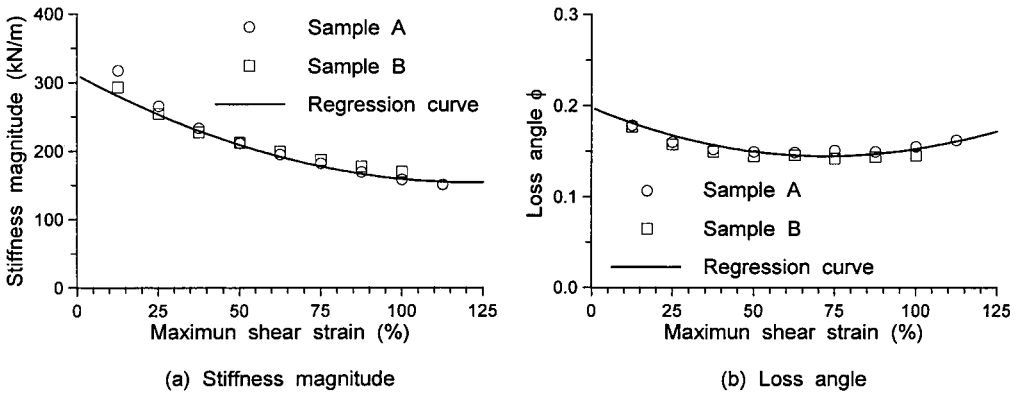

Fig. 16. (a) Stiffness magnitude and (b) loss angle of circular bearing of high-damping rubber varied with maximum shear strain at $P = 140$ kN.

The hysteresis loop of the circular bearing of high-damping rubber obtained from the cyclic shear test of sample B under the compressive force $P = 140$ kN, and the shear strain amplitude $\gamma_{max} = 0.625$ is plotted in Fig. 17 and compared with the loop analyzed from the theoretical model using the material properties of regression. The closeness of the two loops indicates that it is reasonable to assume that the material properties of rubber are constants during a cyclic motion of fixed amplitude.

The variation of height reduction with the horizontal displacement for the circular bearing of high-damping rubber during the cyclic shear test of sample B under the compressive force $P = 140$ kN and the maximum shear strain $\gamma_{max} = 0.625$ is plotted in Fig. 18 and compared with the analytical result calculated from the viscoelastic model using the material properties of regression. Both the experimental and analytical results show that vertical displacement versus horizontal displacement forms a loop in a full cycle of motion. The maximum height reductions for the circular bearing of high-damping rubber under different compressive forces at $\gamma_{max} = 0.625$ are plotted in Fig. 19, which compares the experimental results with the analytical results. Because the vertical displacement is of secondary order to the horizontal displacement, the measured data for height reduction inherently have less accuracy, which leads to a greater deviation of the experimental results from the analytical results.

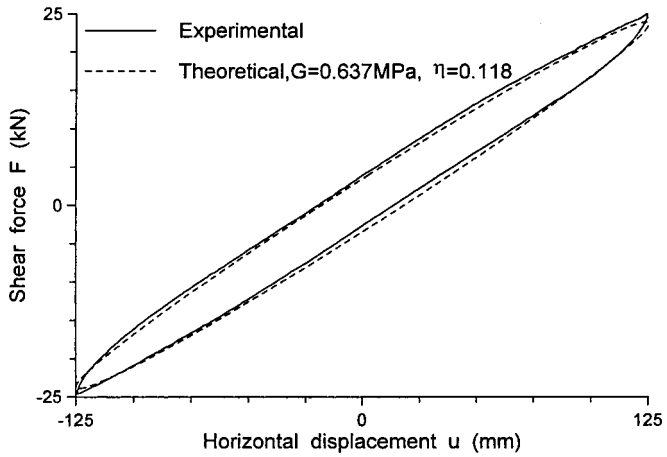

Fig. 17. Hysteresis loop of circular bearing of high-damping rubber, sample B, at $P = 140$ kN and $\gamma_{max} = 0.625$.

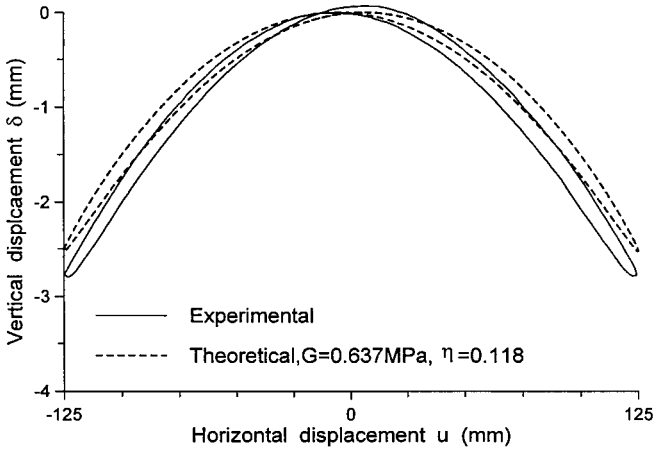

Fig. 18. Vertical displacement loop of circular bearing of high-damping rubber, sample B, at $P = 140$ kN and $\gamma_{max} = 0.625$.

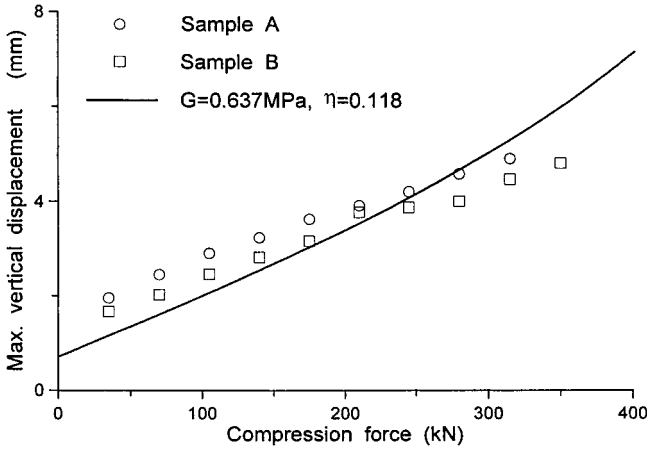

Fig. 19. Height reduction of circular bearing of high-damping rubber varied with compressive force at $\gamma_{max} = 0.625$.

3.3. Normal rubber bearings

The cyclic shear tests on normal rubber bearings were carried out and the similar identification procedures are performed to investigate the variations of the shear modulus G and the loss factor η of the normal rubber with the shear strain amplitude γ_{max}. Fig. 20 shows that the stiffness magnitudes and loss angles obtained from the cyclic shear tests on the square bearings of normal rubber under different compressive forces at the maximum shear strain $\gamma_{max} = 0.75$ fit the curves calculated from the viscoelastic model using the identified material properties. The shear moduli and loss factors identified from the circular and square bearings of the normal rubber are plotted in Fig. 21, from which the quadratic regression of the shear modulus is found as

$$G = 0.8280 - 0.1998\gamma_{max} + 0.07005\gamma_{max}^2 \tag{70}$$

and the quadratic regression for the loss factor is

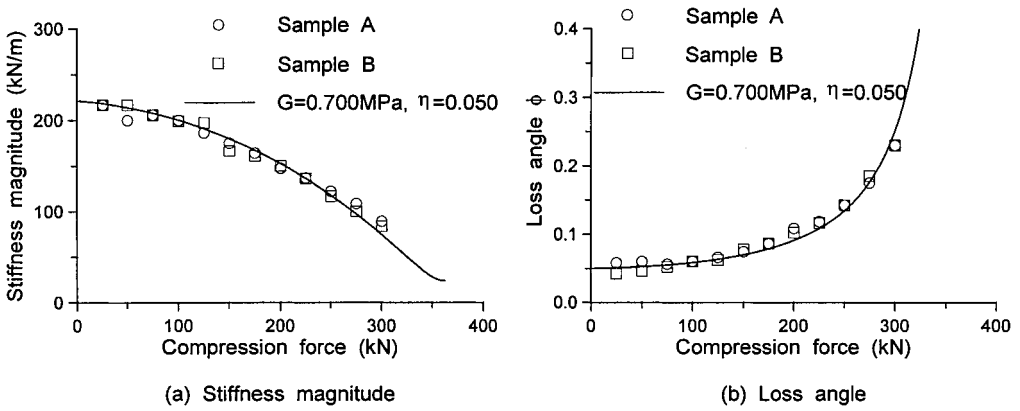

Fig. 20. (a) Stiffness magnitude and (b) loss angle of square bearing of normal rubber varied with compressive force at $\gamma_{max} = 0.75$.

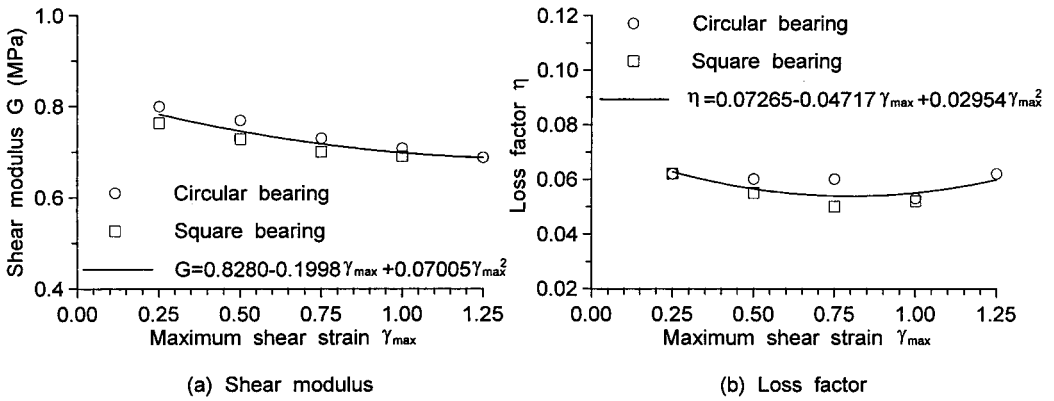

Fig. 21. (a) Shear modulus and (b) loss factor of normal rubber varied with maximum shear strain.

$$\eta = 0.07265 - 0.04717\gamma_{max} + 0.02954\gamma_{max}^2. \tag{71}$$

Compared with the shear modulus and loss factor of the high-damping rubber shown in Fig. 15, the variations of the material properties with the maximum shear strain for the normal rubber have the same tendency as those for the high-damping rubber, but the material properties of the normal rubber are less sensitive to the change of the maximum shear strain.

Substituting Eqs. (70) and (71) into Eqs. (31) and (32), the stiffness magnitude and loss angle varied with the maximum shear strain are plotted in Fig. 22 for the square bearing of normal rubber under the compressive force $P = 100$ kN and compared with the data measured from the cyclic shear tests. The hysteresis loop of the square bearing of normal rubber obtained from the cyclic shear test of sample A under the compressive force $P = 100$ kN and the shear strain amplitude $\gamma_{max} = 1.00$ is plotted in Fig. 23 and compared with the hysteresis loop calculated from the theoretical model using the material properties of regression shown in Eqs. (70) and (71). Figs. 22 and 23 reveal that the behavior of the theoretical model is consistent with the experiment data of normal rubber bearings.

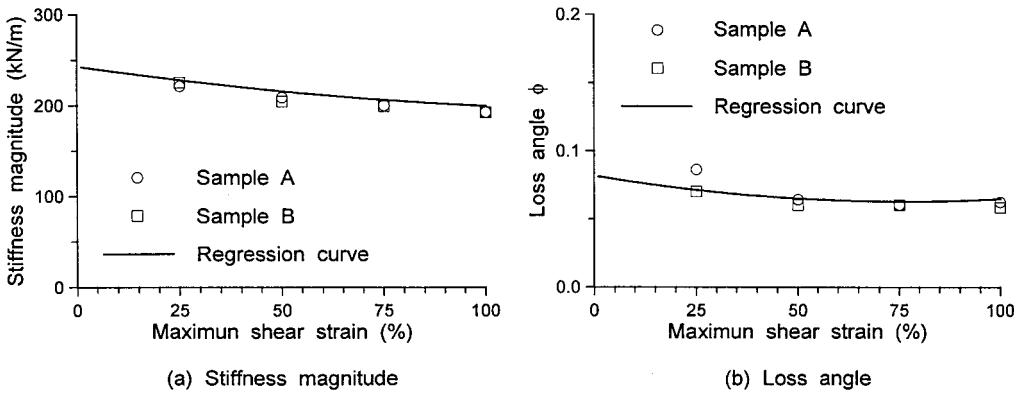

Fig. 22. (a) Stiffness magnitude and (b) loss angle of square bearing of normal rubber varied with maximum shear strain at $P = 100$ kN.

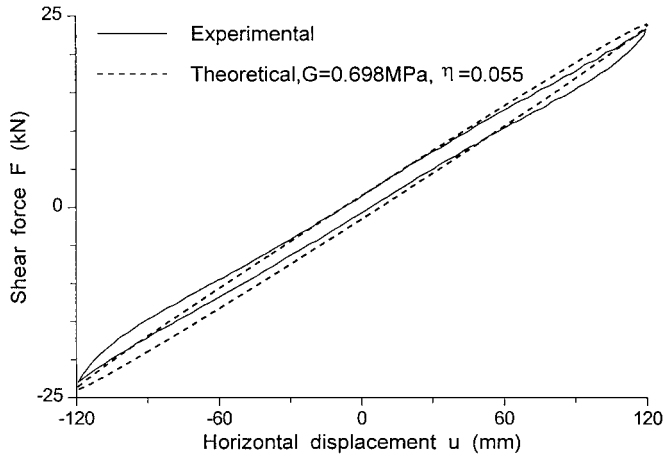

Fig. 23. Hysteresis loop of square bearing of normal rubber, sample A, at $P = 100$ kN and $\gamma_{max} = 1.00$.

3.4. Influence of exciting frequency

The same identification procedure can be applied to study the influence of external exciting frequency on the material properties of rubber. In addition to the varied compressive forces and the varied horizontal displacement amplitudes, the cyclic shear tests on the isolation bearings of high-damping rubber were performed under varied frequencies of horizontal motion. Through the measured data in the tests, the graphs of the stiffness magnitude versus the compressive force and the loss angle versus the compressive force at the specified amplitude and frequency of horizontal displacement are established, from which the shear modulus and loss factor of the high-damping rubber can be identified by the viscoelastic model for that specified amplitude and frequency. Applying two-dimensional regression analysis on these identified parameters, the regression for the shear modulus of high-damping rubber is found as

$$G = 0.892 - 0.722\gamma_{max} + 0.206f_h + 0.436\gamma_{max}^2 - 0.069f_h\gamma_{max} - 0.064f_h^2, \tag{72}$$

where f_h is the frequency of horizontal motion with the unit of Hz. The error of this regression is 0.02563. The regression for the loss factor of high-damping rubber is

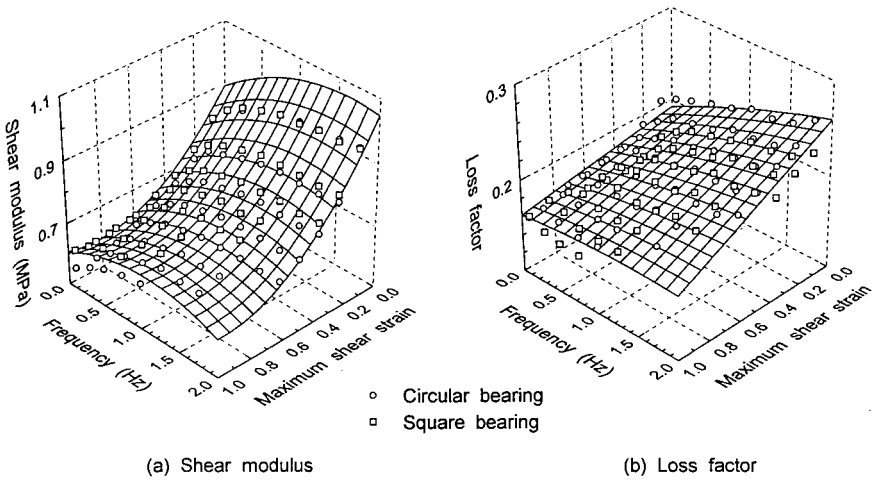

Fig. 24. (a) Shear modulus and (b) loss factor of high-damping rubber varied with frequency and maximum shear strain.

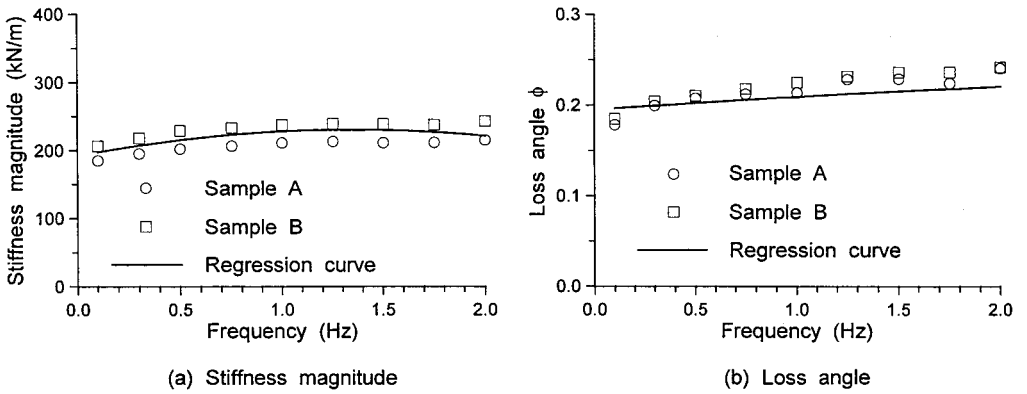

Fig. 25. (a) Stiffness magnitude and (b) loss angle of square bearing of high-damping rubber varied with frequency at $P = 75$ kN and $\gamma_{max} = 0.5$.

$$\eta = 0.192 - 0.029\gamma_{max} + 0.042f_h - 0.001\gamma_{max}^2 - 0.03f_h\gamma_{max} - 0.004f_h^2 \tag{73}$$

of which the error is 0.01430. The surfaces for the regression of shear modulus and loss factor are plotted in Fig. 24 and compared with the values identified from the cyclic shear tests. Substituting Eqs. (72) and (73) into Eqs. (31) and (32), the stiffness magnitude and loss angle of the isolation bearings become functions of compressive force, maximum shear strain and external frequency. For the square bearing of high-damping rubber under the compressive force $P = 75$ kN and the maximum shear strain $\gamma_{max} = 0.5$, Fig. 25 compares the curves of these functions with the stiffness magnitude and the loss angle measured in the cyclic shear tests for the varied exciting frequencies. The theoretical results and experimental results are very close.

4. Conclusions

The steady-state response of the viscoelastic columns, where one end is subjected to both sinusoidal shear force and constant compressive axial load, is solved by the method of separation of variables. The real

part and the imaginary part of the complex horizontal stiffness, denoted as the storage stiffness and the loss stiffness, respectively, are derived and expressed in closed forms, which are numerically consistent with the series solution obtained by the method of mode superposition (Koh and Kelly, 1986, 1989). The derived solution reveals that increasing the compressive axial load will reduce the storage stiffness, which represents the tangential slope of the hysteresis loop at zero strain, and it will enhance the loss stiffness, which is an index of energy dissipation. As the compressive load is increased to reach the buckling load, the column becomes unstable and the storage stiffness is zero. The analytical solution of the buckling load cannot be explicitly derived, but an empirical formula with a very low error is established. Height reduction of the column induced by the horizontal displacement, which is an important parameter in application, is also solved in the closed form.

The material properties of rubber depend on the strain amplitude and the excitation frequency, so that the response of isolation bearings which are made of rubber possesses the same characteristics. However, during the motion of a fixed displacement amplitude and frequency, the response of isolation bearings can be described by the theoretical model of viscoelastic columns with constant shear modulus and constant loss factor. Consequently, the theoretical solution of viscoelastic columns is employed to construct the identification procedure to determine the shear modulus and loss factor of rubber from the cyclic shear tests of isolation bearings. Through this identification procedure, the empirical formulas of shear modulus and loss factor in terms of strain amplitude and excitation frequency are established for two kinds of rubber with different damping characteristics.

Acknowledgements

The research work reported in this article was supported by the National Science Council, Republic of China, under Grant Nos. NSC84-2621-P011-009B and NSC86-2621-P011-002, which is greatly appreciated.

References

American Society for Testing and Materials, 1987. Standard specification for plain and steel-laminated elastomeric bearings for bridges. ASTM Standard D 4014, 487–493.

Cole, J.E., 1979. The effects of frequency, amplitude and load on the dynamic properties of elastomers. Shock and Vibration Bulletin 49, 105–117.

Gent, A.N., Meinecke, E.A., 1970. Compression, bending and shear of bonded rubber blocks. Polymer Engineering and Science 10, 48–53.

Haringx, J.A., 1949. On highly compressible helical springs and rubber rods, and their application for vibration-free mountings, III. Philips Research Reports 4, 206–220.

Kelly, J.M., 1993. Earthquake-Resistant Design with Rubber. Springer, London.

Kelly, J.M., Beucke, K.E., 1983. A friction damped base isolation system with fail-safe characteristics. Earthquake Engineering and Structural Dynamics 11, 33–56.

Kelly, J.M., Celebi, M., 1984. Verification testing of prototype bearings for base-isolated building. Report No. UCB/SESM-84/01, Department of Civil Engineering, University of California, Berkeley.

Koh, C.G., Kelly, J.M., 1986. Effects of axial load on elastomeric isolation bearings. Report No. UCB/EERC-86/12, Earthquake Engineering Research Center, University of California, Berkeley.

Koh, C.G., Kelly, J.M., 1989. Viscoelastic stability model for elastomeric isolation bearings. Journal of Structural Engineering ASCE 115, 285–302.